

Wideband RF Radiance Field Modeling Using Frequency-embedded 3D Gaussian Splatting

Zechen Li^{1*} Lanqing Yang^{1*} Yiheng Bian¹ Hao Pan^{1†}
 Yongjian Fu² Yezhou Wang¹ Zhuxi Chen¹ Yi-Chao Chen¹ Guangtao Xue¹

¹Shanghai Jiao Tong University ²Central South University

{zechlee, yanglanqing, byhbye123, panh09,
 yezhouwang, yichao, gt_xue}@sjtu.edu.cn
 fuyongjian@csu.edu.cn

Abstract

Indoor environments typically contain diverse RF signals distributed across multiple frequency bands, including NB-IoT, Wi-Fi, and millimeter-wave. Consequently, wideband RF modeling is essential for practical applications such as joint deployment of heterogeneous RF systems, cross-band communication, and distributed RF sensing. Although 3D Gaussian Splatting (3DGS) techniques effectively reconstruct RF radiance fields at a single frequency, they cannot model fields at arbitrary or unknown frequencies across a wide range. In this paper, we present a novel 3DGS algorithm for unified wideband RF radiance field modeling. RF wave propagation depends on signal frequency and the 3D spatial environment, including geometry and material electromagnetic (EM) properties. To address these factors, we introduce a frequency-embedded EM feature network that utilizes 3D Gaussian spheres at each spatial location to learn the relationship between frequency and transmission characteristics, such as attenuation and radiance intensity. With a dataset containing sparse frequency samples in a specific 3D environment, our model can efficiently reconstruct RF radiance fields at arbitrary and unseen frequencies. To assess our approach, we introduce a large-scale power angular spectrum (PAS) dataset with 50,000 samples spanning 1 to 94 GHz across six indoor environments. Experimental results show that the proposed model trained on multiple frequencies achieves a Structural Similarity Index Measure (SSIM) of 0.922 for PAS reconstruction, surpassing state-of-the-art single-frequency 3DGS models with SSIM of 0.863.

*Both authors contributed equally.

†Corresponding author.

1. Introduction

Radio frequency (RF) signals constitute various wireless systems that offer numerous conveniences in daily life. For instance, low-frequency NB-IoT (around 1 GHz) is utilized for large-scale interconnection of IoT devices [26]. 5 GHz WiFi/Bluetooth facilitates communication and device connectivity [7], and 77-81 GHz FMCW radar is employed for human motion detection [10]. Efficient comprehension and modelling of these RF signals across wide band can support various downstream tasks [2, 9], including heterogeneous wireless network resource collaborative optimization [1], spectrum sensing and dynamic frequency allocation [11], wideband communication link modeling and optimization [4, 21, 43], as well as cross-band localization and tracking [40]. However, due to the complex nature of RF signal propagation, modeling RF radiance fields remains a significant challenge [23, 31, 33].

Neural radiance fields (NeRF [32]), originally developed for visible light modeling using deep learning, have been extended to RF radiation field reconstruction, seen in Nerf2 [50] and NeWRF [28]. However, these approaches face issues such as high training costs, slow rendering, and limited interpretability [29]. Inspired by 3D Gaussian Splatting (3DGS [12, 13, 15, 22, 25, 34]) technology, researchers have proposed WRF-GS [44] and RF-3DGS [48], which offer ease of training and fast rendering speeds while achieving RF field reconstruction performance comparable to NeRF-based methods. However, although everyday scenarios typically involve broadband RF signals, existing researches focuses primarily on modeling the RF radiation field at a single frequency within a given 3D scene, using training datasets composed of this frequency point [37, 49]. Given that current methods use specific frequency datasets to train models, developing a wideband model based on existing work would require retrain-

ing a model for each new frequency. Additionally, these methods cannot transfer trained models to frequency bands without training datasets, highlighting a key limitation. This raises a research question: Can we design a unified model to model RF radiation fields within a given 3D scene, allowing inference of radiation fields across all frequencies within a broad range?

In electromagnetic (EM) physics, reflection, transmission, and absorption are closely related to a material’s frequency-dependent permittivity and conductivity, while diffraction is highly related to wavelength and obstacle size [8]. Consequently, EM waves of different frequencies exhibit varying propagation behaviors [19], which are strongly frequency-dependent but complex, and are also influenced by the environment’s 3D geometry and material properties.

This paper proposes a frequency embedding-based 3DGS algorithm for unified modeling of wideband RF radiation fields. Based on Huygens’ principle [3], we use 3D Gaussians to represent new wave sources formed when original EM waves encounter obstacles. The EM-related parameters of these Gaussian spheres, such as attenuation factor and signal intensity, are used to describe specific information about these new wave sources. We embed frequency information into the EM-related feature parameters of each 3D Gaussian to model their complex relationships. Specifically, we propose two modules—the attenuation module and the radiance module—to capture the attenuation and signal intensity of each 3D Gaussian at different frequencies and transmitter (TX) antenna’s positions. Once our frequency-embedded 3DGS model is trained with limited frequency points and TX positions, it can determine the parameters of all 3D Gaussian spheres for any TX position and operating frequency. Using projection rendering and differential tile rasterization, it then generates the power angular spectrum (PAS) for a given receiving (RX) antenna array. This enables the model to infer the RF radiance field at unseen frequencies within the wideband and at any transmitter position within the specified 3D environment.

We employ the NVIDIA Sionna software [17] to generate PAS datasets in six indoor environments, covering an ultra-wideband range from 1 GHz to 94 GHz. After being trained on a dataset with limited frequency points and TX positions, our model can successfully predict the PAS for the receiver antenna at unseen frequency points and transmitter positions. Experimental results demonstrate that, when reconstructing the PAS at various TX positions using frequencies in the training dataset, our model achieves an average SSIM improvement of 6.8% compared to state-of-the-art (SOTA) methods trained on a single frequency. These results indicate that our model benefits from the incorporation of cross-frequency information, achieving a better understanding of EM wave propagation and

improved PAS reconstruction in a given 3D environment compared to single-frequency SOTA models. Moreover, our model demonstrates a strong capability in estimating the PAS at unseen frequencies, with performance comparable to single-frequency models trained specifically on data from those unseen frequencies.

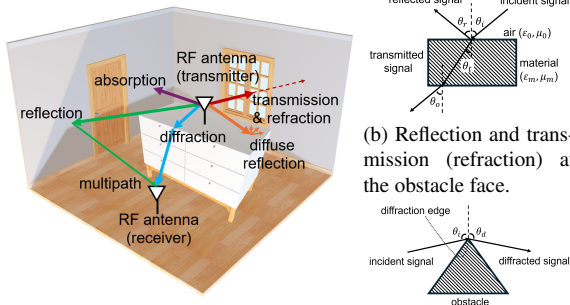
Our contributions are summarized as follows:

- We are the first to propose unified wideband RF radiance field modeling using a frequency-embedded 3DGS model, which can reconstruct PAS for any TX position and frequency in a 3D scene.
- We design the attenuation and radiance network modules with frequency embeddings to learn the frequency-dependent attenuation factor and signal intensity of each 3D Gaussian.
- We generate a wideband PAS dataset (1-94 GHz, 6 indoor environments, 50000 samples in total) and open-source the code and dataset.
- Extensive experiments demonstrate that our model achieves a 6.8% SSIM improvement in PAS prediction over current SOTA methods on trained frequencies and generalizes well to untrained frequencies.

2. Related work

Modeling visible light radiance fields is a hot research area as it supports various computer vision tasks [14]. However, RF radiance fields, with frequencies much lower than visible light, are more complex to model due to their intricate propagation characteristics and multipath effects [20]. Recent studies have explored deep learning for RF radiance field modeling, employing neural networks to learn the complex wireless channel in the environment. Adita et al. [24] introduced LSTM/GRU-based autoencoders to predict the wireless channel quality. Liu et al. [27] proposed FIRE, utilizing variational autoencoders (VAE) to estimate the downlink channel information from the uplink. Inspired by the NeRF [32], several studies have applied it to RF radiance field modeling [28, 35, 48]. Orekondy et al. [35] presented a neural surrogate model based on NeRF to simulate EM propagation behaviors indoors. Zhao et al. [50] proposed NeRF2, a wireless radiance reconstruction method based on NeRF, to predict the PAS at receiver antennas with unmeasured transmitter antenna’s location using channel measurements collected from a real-world indoor environment for training. Lu et al. [28] proposed NeWRF to achieve wireless channel estimation at any unknown positions. However, NeRF-based methods often encounter challenges such as high computational complexity and slow synthesis speeds.

Considering the advantages of 3DGS over NeRF, Wen et al. proposed WRF-GS [44], a method that substitutes the NeRF core in NeRF2 with 3DGS to enable fast training and rendering for the PAS reconstruction task. Zhang



(a) Complex propagation behaviors of the EM waves. (b) Reflection and transmission (refraction) at the obstacle face. (c) Diffraction phenomenon happened at the obstacle edge.

Figure 1. EM waves exhibit complex propagation behaviors that are closely influenced by factors such as materials, wavelengths, and the shapes of obstacles.

et al. presented RF-3DGS [48], which uses 3DGS to reconstruct a dense wireless channel with limited measured receiving samples, given a specific 3D environment and a fixed transmitter antenna. Yang et al. proposed GSRF [47], which uses 3D Gaussian spheres with complex-valued attributes and integrates an RF-specific CUDA-enabled ray tracing algorithm for efficient PAS reconstruction.

While existing research only focuses on single-frequency scenarios, wideband RF radiance field modeling remains insufficiently explored. To address this issue, we first investigate the dependence of EM wave propagation on frequency in a specific 3D environment, based on fundamental physics. Subsequently, we propose a frequency-embedded 3DGS model for unified modeling and reconstruction of wideband RF radiance fields.

3. Preliminary

3.1. Primer on electromagnetics

RF radiation field reconstruction involves using sparse RF signal samples from a given environment to reconstruct the radiance field throughout the area. The reconstruction algorithm is required to understand various EM wave propagation behaviors such as reflection, transmission, refraction, diffraction, and absorption. Moreover, the multipath effect occurs when EM waves from the same transmitting (TX) antenna travel along multiple paths and combine at the receiving (RX) antenna; this effect can lead to signal enhancement or attenuation. The complex propagation behaviors, as shown in Fig. 1(a), make RF modeling more challenging than modeling visible light. In this section, we systematically analyze the various propagation behaviors of electromagnetic waves and investigate how they are influenced by frequency, 3D geometry, and material properties.

As EM waves travel through the air with a distance d , their path loss is influenced by the frequency (f): $pathloss = 20 \log_{10} \frac{4\pi df}{c}$, where c is the speed of light.

When encountering an obstacle, as shown in Fig. 1(b), waves may reflect, transmit, or be absorbed. This behavior is primarily determined by the material's permittivity (ϵ_m) and conductivity (μ_m). Utilizing equivalent circuit models [18] and S-parameter formulas [5], we can derive reflection rate (R) as $R = \left| \frac{\sqrt{\eta_m} - \sqrt{\eta_0}}{\sqrt{\eta_m} + \sqrt{\eta_0}} \right|^2$, transmission rate (T) as $T = \left| \frac{2\sqrt{\eta_0}}{\sqrt{\eta_m} + \sqrt{\eta_0}} \right|^2$, and absorption (A) as: $A = 1 - R - T$. Among them, $\eta_m = \frac{\mu_m}{\epsilon_m}$, $\eta_0 = \frac{\mu_0}{\epsilon_0}$, where ϵ_0 and μ_0 are the permittivity and conductivity of the air. We can derive the relationship between the angle of refraction (i.e., transmission in the obstacle) θ_t and the angle of incidence θ_i : $\frac{\sin(\theta_t)}{\sin(\theta_i)} = \sqrt{\frac{\epsilon_m \mu_m}{\epsilon_0 \mu_0}}$. It is important to note that these parameters, ϵ and μ , of any material depend on frequency and can be represented as $\epsilon(f)$ and $\mu(f)$ [16]. **Thus, we conclude that reflection, transmission (refraction), and absorption of EM waves when encountering obstacles are related to a material's frequency-dependent properties.**

When EM waves encounter the edges of an obstacle, diffraction occurs, as shown in Fig. 1(c). Using the Uniform Theory of Diffraction (UTD) [41], we can express the relationship between the diffracted EM field (E_d) and the incident field (E_i) in a simplified form: $E_d = E_i D(\theta_i, \theta_d, k, \epsilon_m, \mu_m) F$, where θ_i is the incident angle, θ_d is the diffracted angle, k is wavenumber: $k = \frac{2\pi f}{c}$. The diffraction factor $D(\cdot)$ describes changes in an EM wave's amplitude and phase as it passes an edge, and F represents a polarization factor. **Thus, we can also conclude that the characteristics of diffraction when EM waves encounter the obstacles are strongly correlated with both the frequency of the EM wave and the 3D geometry of the edges.**

3.2. 3D Gaussian representation in EM domain

According to the Huygens-Fresnel principle [30], each point on an EM wavefront acts as a secondary source, with propagation being the superposition of these secondary sources. When EM waves encounter obstacles, their propagation changes significantly, creating new EM radiation sources with distinct properties. Therefore, the 3DGS technique is highly suitable for representing RF radiation field, as it involves modeling each 3D point on an object's surface or edge as a 3D Gaussian and capturing the new source characteristics when the EM waves meet that point. The 3D Gaussian encompasses not only position, rotation, and weight related to its spatial attributes but also EM-related characteristics such as the attenuation factor and RF signal radiance intensity. Specifically, the signal intensity refers to the EM energy produced when the Gaussian sphere acts as a secondary wave source. The attenuation factor describes each Gaussian sphere's hierarchical influence on EM waves reaching the receiving antenna, reflecting its role in the overall wave superposition. Thus, the EM propagation behaviors at each 3D point can be directly modeled using spe-

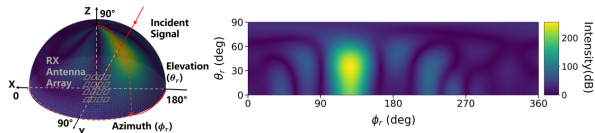


Figure 2. An example of the power angular spectrum.

cific parameters of the 3D Gaussian.

3.3. Power angular spectrum

The RF radiation field describes the spatial distribution and propagation characteristics of EM waves. However, specific modeling often employs representations like wireless channels or the power angular spectrum (PAS) to characterize these fields. In this paper, we draw on NeRF2 [50] and WRF-GS [44] to apply a PAS reconstruction task for assessing the model’s capability in RF radiation field modeling. Fig. 2 illustrates an example of a PAS, with the top part showing a 3D view centered on the receiving antenna array to depict the spatial angular distribution of EM waves; the bottom part is a 2D representation where the x and y axes represent azimuth and elevation angles, and color indicates RF signal energy. In this work, we define the azimuth angle range as $0 \sim 360^\circ$ and the elevation angle range as $0 \sim 90^\circ$ for hemispherical radiation of the receiving antenna’s direction. Thus, the PAS image dimensions are 90×360 , with each pixel representing energy information.

4. Method design

4.1. Overview

Modeling task: Our objective is unified modeling of wideband RF radiation fields. In a 3D environment with a pair of TX and RX antennas, training data are collected by moving a limited number of TX antennas, each operating at different frequency points, across discrete spatial positions. At each location, the active TX antenna emits EM waves, and the corresponding RX phased array antenna records the wideband PAS. The task is to leverage the measured PAS data, collected at finite frequency points and positions, to train a model that can reconstruct the PAS at the fixed RX antenna for any TX antenna position and any RF frequency within the scene.

Our approach: Our model is based on 3DGS technology and incorporates frequency embedding modules to learn the complex relationship between EM wave propagation behavior and frequency in each 3D Gaussian sphere. As illustrated in Fig. 3, our proposed model consists of two parts: a 3DGS model for PAS synthesis and a frequency-embedded EM feature network for learning the key parameters related to EM propagation within the 3D Gaussians.

We initialize the positions of the 3D Gaussians based on point cloud information from the 3D scene, while other Gaussian properties are either randomly initialized or assigned default values. The EM feature network takes as input the position of the TX antenna, the frequency value, and the positions of the 3D Gaussians, and then outputs the frequency-embedded EM propagation-related parameters, i.e., the attenuation factors and signal intensities, for all 3D Gaussians. By using a tile-based differentiable rasterizer, 3D Gaussians are splatted onto the projected RX view hemisphere to predict the PAS. During training, the loss gradient between the predicted PAS and the simulated ground truth PAS is propagated backwards to update the Gaussian properties and the parameters of the EM feature network.

4.2. Frequency-embedded EM feature parameter module

Considering that each 3D Gaussian represents a part of the object (e.g., mesh or edge), when an incident EM wave excites a 3D Gaussian, its characteristics, such as attenuation (δ) and signal intensity (Sig), change according to the properties of the EM waves. Firstly, the position of the TX determines the incident direction of the EM waves, which influences reflection, diffraction, and other related directions. Secondly, the frequency-dependent nature of material properties, such as relative permittivity and conductivity, affects the ratios of reflection and transmission. As a result, the attenuation and signal intensity characteristics, referred to as EM propagation features, are influenced by both the position and the operational frequency of the transmitting antenna. Conversely, the spatial features of the Gaussians, such as position, scaling, and rotation, remain invariant. This stability enables the use of machine learning methods to effectively capture the dynamically changing, frequency-dependent EM feature parameters. Thus, we design a frequency-embedded EM feature network, which can be expressed as follows:

$$F_{\Theta} : (P(G), P(TX), freq) \rightarrow (\delta(G, freq), Sig(G, freq)) \quad (1)$$

All the inputs, 3D Gaussians’ positions, TX antenna’s position, and the frequency, are embedded into vectors by positional encoding, then fed into the EM feature network, which is composed of several fully-connected layers. The first half of the EM feature network takes the Gaussians $P(G)$ and the signal frequency $freq$ as input, and outputs the hidden EM feature vector $h(G)$. Subsequently, the Gaussian attenuation $\delta(G)$ is derived from the $h(G)$ through a two-layer MLP:

$$F_{\Theta_1} : (P(G), freq) \rightarrow (h(G, freq), \delta(G, freq)) \quad (2)$$

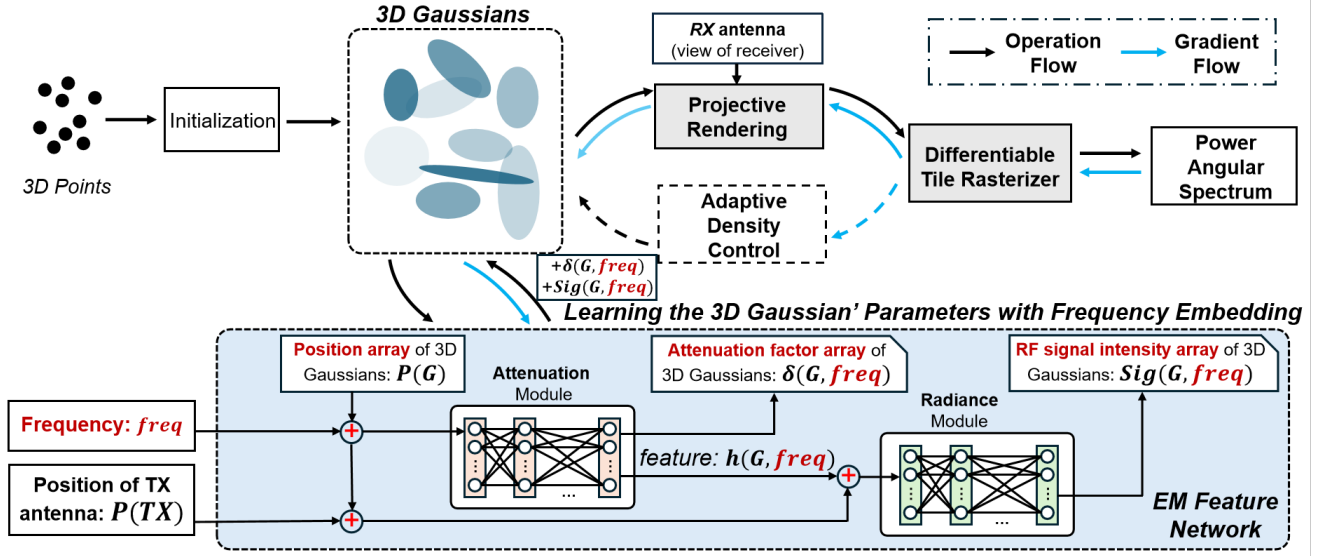


Figure 3. Architecture of the frequency embedding-based 3D Gaussian Splatting model.

The structure of the second half of the EM feature network is similar to the first half, with the Gaussians $P(G)$, the TX position $P(TX)$, the signal frequency $freq$ and the hidden vector $h_2(G)$ with TX position information. Through another two-layer MLP, the network outputs the RF signal intensity $Sig(G)$:

$$F_{\Theta_2} : (P(G), P(TX), freq, h(G, freq)) \rightarrow (h_2(G, freq), Sig(G, freq)) \quad (3)$$

4.3. RX view projection

The PAS represents the received signal distribution of RX antenna array on a hemisphere, but the synthesis plane of 3DGS is the view projection plane of a camera. Therefore, a virtual camera imaging plane is constructed based on the RX position and orientation, then an indirect projection from the camera imaging plane onto the hemisphere of the RX array is applied.

Given a point $\mathbf{P} = (x, y, z)$ in the Cartesian coordinates ($z \geq 0$), the target is to project it onto the spatial spectrum hemisphere, where the corresponding angle pixel is represented as $p = (p_x, p_y)$. The azimuth angle $\phi \in [-\pi, \pi]$ and the zenith angle $\theta \in [0, \pi/2]$ can be obtained by $\phi = atan2(x, y) = sgn(y)arctan(y/x)$ and $\theta = arccos(z/r)$, where $atan2(\cdot)$ is the four-quadrant inverse tangent function, $sgn(\cdot)$ is the sign function, and $r = \sqrt{x^2 + y^2 + z^2}$ is the Euclidean distance between P and the Cartesian origin. Then the angles can be scaled and shifted into the spectrum resolution range with $p_x = \frac{\phi + \pi}{\pi}W$ and $p_y = \frac{\theta}{\pi/2}H$, where $W \times H$ is the spectrum resolution.

4.4. Power angular spectrum rendering

After 3D Gaussians are projected onto the spectrum hemisphere as 2D Gaussians, these 2D Gaussians can be used to render the PAS, similar to the differentiable tile-based rasterization algorithm of the optical 3DGS model. Since each 2D Gaussian can affect multiple pixels, splitting the PAS into tiles containing adjacent pixels instead of fine-grained pixels for parallel rendering can speed up the PAS synthesis.

Typically each Gaussian may cover multiple tiles while each tile contains multiple Gaussians. For each 2D Gaussian, if it covers t tiles, it will be instantiated t times with a key combining its view depth and tile ID. Then these Gaussian instances are sorted by the key, creating a depth-increasing order corresponding to each tile.

For each pixel within a tile, the value of EM signal is accumulated according to the Gaussians covering it. Assuming that a pixel contains N Gaussians, the signal $Sig(G_i)$ of a Gaussian G_i should be attenuated by its former Gaussians' attenuation δ , which is between G_i and the RX. Therefore, the value of the pixel p is:

$$I(p) = \sum_{i=1}^N \left(\prod_{j=1}^{i-1} \delta(G_j) \right) \times Sig(G_i) \quad (4)$$

Leveraging the output EM features from the EM feature network, we treat the attenuation factor δ_f and the signal intensity Sig_f with frequency and TX position information as a modification to the original Gaussians' attenuation δ_o and signal attributes Sig_o . Therefore, $\delta_o + \delta_f$ is used as the final attenuation factor, while $Sig_o + Sig_f$ as the final signal intensity. This allows us to update the final attenuation factor and signal intensity in 3D Gaussians by learn-

ing the residual values, ensuring the model more stably and accurately reflects changes in attenuation and signal characteristics. Thus, for the final PAS rendering and training processes, we modify Eq. 4 as follows:

$$I(p) = \sum_{i=1}^N \left(\prod_{j=1}^{i-1} (\delta_o(G_j) + \delta_f(G_j, \mathbf{freq})) \right) \times (\text{Sig}_o(G_i) + \text{Sig}_f(G_i, \mathbf{freq})) \quad (5)$$

4.5. Model training

Initiated from the scenario point clouds, the Gaussians adaptively control their density every few epochs to better reconstruct the objects in the space [46]. If a Gaussian’s positional gradients are large, it means that this Gaussian is not well-reconstructed yet. Small Gaussians indicate under-reconstruction, so they are cloned and the cloned Gaussian is moved along the direction of positional gradients, while large Gaussians imply over-reconstruction, and they are split into two smaller ones sampled from the original Gaussian. Every certain epochs, if a Gaussian’s attenuation factor δ is less than a threshold ϵ_δ , the Gaussian will be removed, as it is considered to make minimal contributions. In addition, the δ of each Gaussian is reset close to zero every few epochs as a strategy for adaptive density control and removal of useless Gaussians. The parameters of the 3D Gaussians and EM feature network are optimized by stochastic gradient descent (SGD) and the loss between predicted PAS and ground truth.

The L1-loss is the simplest loss for the model optimization. Since the structural similarity index measure (SSIM) measures the structural similarity of two images, it is a suitable measurement for PAS prediction[]. Note that the Gaussian’s attenuation reset operation may lead to divergence because the EM feature δ_f from the network is much larger than the reset original attenuation of Gaussians, we add an L2-norm penalty for the δ_f term to avoid this potential divergence issue. Therefore, the final loss function is a combination of the \mathcal{L}_1 loss, the SSIM loss and an L2-penalty, where λ is set to 0.2 and λ_δ is set to 0.01:

$$\mathcal{L} = (1 - \lambda)\mathcal{L}_1(\text{PAS}_{\text{pred}}, \text{PAS}_{\text{GT}}) + \lambda\mathcal{L}_{\text{SSIM}}(\text{PAS}_{\text{pred}}, \text{PAS}_{\text{GT}}) + \lambda_\delta\mathcal{L}_2(\delta_f) \quad (6)$$

5. Evaluation

5.1. Dataset description and experiment setup

Currently, there is no dataset available that supports the task of PAS reconstruction across wideband. To address this, we construct a large-scale simulated wideband angle power spectrum dataset that spans the frequency range of 1-94 GHz and includes 6 different indoor scenarios. Specifically, in a 3D environment, we utilize the NVIDIA Sionna

simulator [17] to model the propagation of EM waves emitted by the TX antenna, and employ the Bartlett beam forming method provided by NeRF2 [50] to generate PAS images at the location of the RX antennas. In the simulation settings, the RX is a 4×4 antenna array with each antenna being directional, while the TX antenna is a single omnidirectional antenna. In each 3D scenario, we uniformly sample 900 different TX positions and remove the inaccessible ones, allowing the RX to receive diverse signals from TX at various positions. For each TX position, we adjust the frequencies of the TX, the RX, and the materials’ permittivity and conductivity to simulate the propagation behavior of EM waves at different frequencies and generate the corresponding PAS data. In six different scenarios, we select 10 common frequency points and generate the corresponding PAS datasets. Additionally, to study the impact of a larger number of frequency points on our model’s ability to perform wideband RF radiance field modeling, we select one scenario and simulate 21 frequency points that are uniformly distributed between 1 and 94 GHz. For detailed information on the data generation process and the specific parameter settings of the Sionna software, please refer to the supplementary material.

For each 3D environment, we use wideband PAS images to train our proposed frequency-embedded 3DGS model and reconstruct the RF radiance field. Specifically, we divide the PAS image dataset according to the TX positions, with 80% used for training and 20% for testing. This means all frequency points in the scenario share the same training/testing TX position. Additionally, we divide the frequencies into a training set and a testing set to validate our model’s reconstruction ability at previously unseen frequencies. We use the Structural Similarity Index (SSIM [42]) between the predicted PAS image and the simulated ground truth as a criterion for quantitatively evaluating the model’s performance.

Our model is implemented in Python, with both training and rendering conducted on an NVIDIA A800 GPU equipped with 80 GB of graphics memory. For access to the code, please refer to the supplementary material.

5.2. Overall evaluation

To validate the performance of our system, we design a series of experiments to compare it with the current SOTA method, WRF-GS+ [45] and GSRF [47]. Since WRF-GS+ and GSRF can only reconstruct PAS at a single frequency, we conduct experiments on our datasets across 6 scenarios at 10 frequencies. For each 3D scenario, we train a specific WRF-GS+ and GSRF model for each frequency and assess its performance on the corresponding test set. In contrast, for each 3D scenario, we train our frequency-embedded 3DGS model using data from all 10 frequencies and then evaluate its performance using test sets from all

Table 1. Overall evaluation in 6 scenes at 10 frequencies.

Scene	Model	Median SSIM at 10 single frequencies										
		1	2.4	5	10	24.25	37	47	60	77	94	Avg.
1	WRF-GS+	0.898	0.890	0.896	0.905	0.884	0.886	0.867	0.901	0.883	0.888	0.890
	GSRF	0.714	0.666	0.703	0.687	0.706	0.721	0.629	0.689	0.672	0.674	0.686
	Ours	0.922	0.928	0.928	0.932	0.934	0.926	0.932	0.929	0.932	0.930	0.929
2	WRF-GS+	0.785	0.836	0.782	0.849	0.884	0.891	0.890	0.899	0.894	0.764	0.874
	GSRF	0.649	0.614	0.641	0.668	0.682	0.687	0.682	0.684	0.603	0.699	0.661
	Ours	0.926	0.933	0.936	0.942	0.949	0.951	0.949	0.951	0.953	0.954	0.944
3	WRF-GS+	0.897	0.864	0.888	0.874	0.859	0.879	0.880	0.899	0.871	0.885	0.880
	GSRF	0.629	0.589	0.607	0.618	0.646	0.635	0.626	0.649	0.639	0.641	0.628
	Ours	0.926	0.923	0.929	0.929	0.927	0.933	0.929	0.933	0.931	0.921	0.928
4	WRF-GS+	0.819	0.826	0.853	0.840	0.859	0.867	0.847	0.831	0.847	0.858	0.845
	GSRF	0.673	0.683	0.682	0.689	0.692	0.698	0.7	0.69	0.692	0.676	0.688
	Ours	0.921	0.916	0.939	0.941	0.937	0.929	0.937	0.934	0.935	0.933	0.932
5	WRF-GS+	0.774	0.787	0.810	0.835	0.870	0.840	0.836	0.871	0.837	0.855	0.832
	GSRF	0.597	0.531	0.558	0.577	0.583	0.609	0.597	0.596	0.568	0.561	0.578
	Ours	0.796	0.870	0.888	0.888	0.895	0.883	0.898	0.893	0.893	0.883	0.879
6	WRF-GS+	0.845	0.846	0.843	0.842	0.857	0.873	0.862	0.863	0.880	0.879	0.859
	GSRF	0.646	0.61	0.599	0.643	0.597	0.637	0.642	0.639	0.602	0.623	0.624
	Ours	0.911	0.911	0.920	0.915	0.924	0.922	0.931	0.927	0.932	0.920	0.921

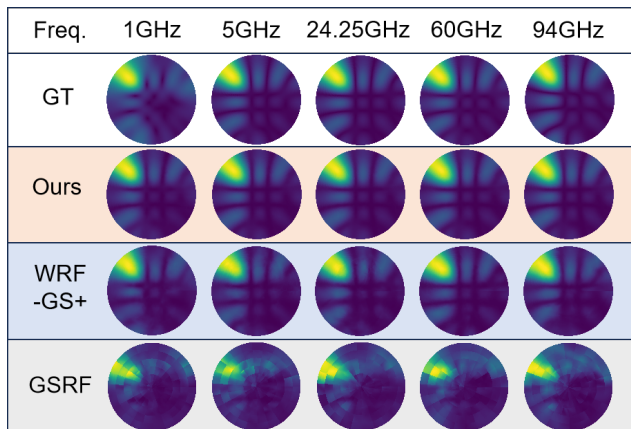


Figure 4. Example of PAS reconstruction at diverse frequencies.

these frequencies.

Tab. 1 presents the detailed results of the comparative experiments. Statistical analysis shows that our method achieves an average PAS prediction SSIM of 0.922 across all frequencies, whereas the 10 specifically trained SOTA models have an average prediction SSIM of 0.863, resulting in an improvement of 6.8%. Fig. 4 presents partial visual results of PAS reconstruction. It demonstrates that our method not only surpasses the current SOTA in terms of the SSIM measurement, but also reconstructs PAS with better visual quality.

Based on the experimental results, we draw the following

Table 2. Cross-frequency prediction in 6 scenes at 10 frequencies with different training/test combinations.

Scene	C1	C2	C3
1	0.936	0.930	0.923
2	0.960	0.956	0.943
3	0.941	0.937	0.928
4	0.954	0.950	0.936
5	0.913	0.898	0.859
6	0.927	0.921	0.912

findings: (1) By designing a unified wideband 3DGS model, we can effectively model the RF radiance fields across different frequency bands; (2) Our frequency-embedded 3DGS model, trained on multi-frequency PAS data, outperforms single-frequency-trained SOTA 3DGS models. These phenomena indicate that a model capable of understanding RF radiation fields across multiple frequency bands can achieve a deeper comprehension of EM wave propagation behavior at any specific frequency in a 3D scenario.

5.3. Cross-frequency prediction

To explore our model’s ability to predict the PAS at unknown (i.e., untrained) frequencies, we conducted cross-frequency experiments across all 6 scenes, selecting several frequencies out of 10 frequencies as training frequencies, while the remaining frequencies were used for testing. For

Table 3. Wideband prediction performance on unseen positions or unseen frequencies in 6 scenes.

Scene	Test-set-1	Test-set-2	Test-set-3
1	0.931	0.931	0.928
2	0.957	0.954	0.950
3	0.938	0.934	0.929
4	0.951	0.946	0.937
5	0.917	0.905	0.900
6	0.925	0.924	0.921

example, C1 is the combination of 5 frequencies for training and the other 5 frequencies for test. C2 consists of 3 training frequencies and 7 test frequencies, and C3 consists 2 training frequencies and 8 test frequencies. Note that in this experiment, we use all the TX positions for training across frequencies.

The results of the cross-frequency experiments are presented in Tab. 2. The results demonstrate that (1) our model can accurately predict the PAS in a given environment at untrained frequency bands, (2) our model works efficiently when trained on only 2 different frequencies, and (3) using more training frequencies improves the performance and stability of our model.

5.4. Performance on unseen positions and unseen frequencies

To figure out whether spatial information (i.e. TX position trained or not) or frequency information (i.e. frequency trained or not) has more impact on the reconstruction of the wideband RF radiance field, we further split the whole dataset into 4 parts: part 1 is the training set containing 5 frequencies (i.e. known frequencies), with 80% samples (i.e. known TX positions); part 2 as test-set-1 containing the remaining 20% samples at these 5 frequencies (i.e. known frequency, unknown position); part 3 as test-set-2 containing other 5 untrained frequencies with 80% samples (i.e. unknown frequency, known position); and part 4 as test-set-3 containing the last 20% samples at those 5 untrained frequencies (i.e. unknown frequency, unknown position).

The experimental results are shown in Tab. 3. All the results in the six scenes consistently indicate that the PAS prediction is more difficult at unseen frequencies than unseen TX positions. However, even when either TX position or frequency is unseen in the training set, our wideband model performs comparably to trained samples with trained TX position or frequency, showing high stability and robustness.

5.5. Training and inference efficiency

We compared the efficiency of our wideband model with SOTA and GSRF on an NVIDIA A800 GPU, as shown in

Table 4. Comparison on training, inference and rendering cost.

	Training	Inference	Rendering
Ours	120.7min	9.2ms	6.7ms
WRF-GS+	73.2min	5.0ms	1.3ms
GSRF	133.3min	26.6ms	--

Table 5. Ablation study of two frequency-embedded feature, \checkmark/\times denotes with/without the feature. *Div* means that the model does not converge.

Module		SSIM	
δ_f	Sig_f	All freq.	Cross freq.
\checkmark	\checkmark	0.922	0.927
\times	\checkmark	0.920	0.927
\checkmark	\times	<i>Div</i>	<i>Div</i>
\times	\times	<i>Div</i>	<i>Div</i>

Tab. 4. By introducing the frequency-embedding EM feature network, our model incurs an acceptable amount of overhead in training and inference, while delivering an improvement in PAS reconstruction quality and the capability for PAS prediction on untrained frequencies.

5.6. Ablation study

Our system incorporates frequency embeddings to learn the attenuation and signal features of the 3D Gaussians. To evaluate the advantages of our proposed EM feature network with frequency embedding, we conduct ablation study on these two frequency-embedded features. The results are summarized in Tab. 5, where we compare the performance of PAS reconstruction when predicting at all training frequencies or unknown frequencies. While not using frequency-embedding may cause model training divergence, both frequency-embedded features used together further enhance PAS prediction, indicating the significant improvement for PAS reconstruction that benefits from frequency information.

6. Discussion and conclusion

In this paper, we propose a novel frequency-embedded 3DGS model to efficiently model RF radiation fields across a wideband. Our approach utilizes attenuation and radiation modules to learn frequency-dependent features within 3D Gaussians, capturing the complex relationship between the EM wave propagation and the frequency.

Acquiring wideband PAS data presents significant challenges, as it requires multiple models of transmitting antennas, as well as phased array receivers, signal sources, and spectrum analyzers that operate across different frequency bands. We utilize the NVIDIA Sionna simulator

to generate a large-scale simulated wideband PAS dataset and conduct extensive experiments to validate our method's effectiveness. Although there is a gap between simulated and real-world data [39], Sionna, based on rigorous physical formulas, can accurately simulate the differences in EM wave propagation behavior across different frequency bands [6, 17, 36, 38]. Thus, our experimental results can affirm the feasibility of utilizing a unified model to represent wideband EM wave propagation behavior.

References

- [1] Hayder Faeq Alhashimi, MHD Nour Hindia, Kaharudin Dimiyati, Effariza Binti Hanafi, Nurhizam Safie, Faizan Qamar, Khairul Azrin, and Quang Ngoc Nguyen. A survey on resource management for 6g heterogeneous networks: current research, future trends, and challenges. *Electronics*, 12(3):647, 2023. 1
- [2] Zhenlin An, Longfei Shangguan, John Kaewell, Philip Pietraski, and Kyle Jamieson. Radiotwin: A digital building material twin for wideband, cross-link, cross-band wireless channel prediction. In *2025 IEEE International Symposium on Dynamic Spectrum Access Networks (DySPAN)*, pages 1–10. IEEE, 2025. 1
- [3] Bevan B Baker and Edward Thomas Copson. *The mathematical theory of Huygens' principle*. American Mathematical Soc., 2003. 2
- [4] Avishek Banerjee, Xingya Zhao, Vishnu Chhabra, Kannan Srinivasan, and Srinivasan Parthasarathy. Horcrux: Accurate cross band channel prediction. In *Proceedings of the 30th Annual International Conference on Mobile Computing and Networking*, pages 1–15, 2024. 1
- [5] Fritz Caspers. Rf engineering basic concepts: S-parameters. *arXiv preprint arXiv:1201.2346*, 2012. 3
- [6] Jiechen Chen, Sangwoo Park, Petar Popovski, H Vincent Poor, and Osvaldo Simeone. Neuromorphic split computing with wake-up radios: Architecture and design via digital twinning. *IEEE Transactions on Signal Processing*, 2024. 9
- [7] H.W. Cho and K.G. Shin. Drew: Double-throughput emulated wifi. In *Proceedings of the 30th Annual International Conference on Mobile Computing and Networking*, pages 663–678. ACM, 2024. 1
- [8] John Maxwell Cowley. *Diffraction physics*. Elsevier, 1995. 2
- [9] C. De Alwis, A. Kalla, Q.V. Pham, et al. Survey on 6g frontiers: Trends, applications, requirements, technologies and future research. *IEEE Open Journal of the Communications Society*, 2:836–886, 2021. 1
- [10] F. Ding, Z. Luo, P. Zhao, et al. Milliflow: Scene flow estimation on mmwave radar point cloud for human motion sensing. In *European Conference on Computer Vision*, pages 202–221, Cham, 2024. Springer Nature Switzerland. 1
- [11] Xuechao Fan. Intelligent radio spectrum management and dynamic spectrum allocation algorithm. In *2024 International Conference on Power, Electrical Engineering, Electronics and Control (PEEEEC)*, pages 836–841. IEEE, 2024. 1
- [12] Z. Fan, K. Wang, K. Wen, et al. LightGaussian: Unbounded 3D Gaussian Compression with 15x Reduction and 200+ FPS. *Advances in Neural Information Processing Systems*, 37:140138–140158, 2024. 1
- [13] G. Fang and B. Wang. Mini-Splatting: Representing Scenes with a Constrained Number of Gaussians. In *European Conference on Computer Vision*, pages 165–181, Cham, 2024. Springer Nature Switzerland. 1
- [14] Kyle Gao, Yina Gao, Hongjie He, Dening Lu, Linlin Xu, and Jonathan Li. Nerf: Neural radiance field in 3d vision, a comprehensive review. *arXiv preprint arXiv:2210.00379*, 2022. 2
- [15] S. Girish, K. Gupta, and A. Shrivastava. Eagles: Efficient Accelerated 3D Gaussians with Lightweight Encodings. In *European Conference on Computer Vision*, pages 54–71, Cham, 2024. Springer Nature Switzerland. 1
- [16] David J. Griffiths. *Introduction to Electrodynamics*. Pearson, 3rd edition, 1999. 3
- [17] Jakob Hoydis, Sebastian Cammerer, Fayçal Ait Aoudia, Avinash Vem, Nikolaus Binder, Guillermo Marcus, and Alexander Keller. Sionna: An open-source library for next-generation physical layer research. *arXiv preprint arXiv:2203.11854*, 2022. 2, 6, 9
- [18] Xiaosong Hu, Shengbo Li, and Huei Peng. A comparative study of equivalent circuit models for li-ion batteries. *Journal of Power Sources*, 198:359–367, 2012. 3
- [19] Akira Ishimaru. *Electromagnetic wave propagation, radiation, and scattering: from fundamentals to applications*. John Wiley & Sons, 2017. 2
- [20] Wen Jiang, Boshu Lei, and Kostas Daniilidis. Fisherrf: Active view selection and uncertainty quantification for radiance fields using fisher information. *arXiv preprint arXiv:2311.17874*, 2023. 2
- [21] Wei Jiang, Qiheng Zhou, Jiguang He, Mohammad Asif Habibi, Sergiy Melnyk, Mohammed El-Absi, Bin Han, Marco Di Renzo, Hans Dieter Schotten, Fa-Long Luo, et al. Terahertz communications and sensing for 6g and beyond: A comprehensive review. *IEEE Communications Surveys & Tutorials*, 26(4):2326–2381, 2024. 1
- [22] Bernhard Kerbl, Georgios Kopanas, Thomas Leimkühler, and George Drettakis. 3d gaussian splatting for real-time radiance field rendering. *ACM Trans. Graph.*, 42(4):139–1, 2023. 1
- [23] Robert G Kouyoumjian and Prabhakar H Pathak. A uniform geometrical theory of diffraction for an edge in a perfectly conducting surface. *Proceedings of the IEEE*, 62(11):1448–1461, 2005. 1
- [24] Adita Kulkarni, Anand Seetharam, Arti Ramesh, and J Dinal Herath. Deepchannel: Wireless channel quality prediction using deep learning. *IEEE Transactions on Vehicular Technology*, 69(1):443–456, 2019. 2
- [25] J. C. Lee, D. Rho, X. Sun, et al. Compact 3D Gaussian Representation for Radiance Field. In *IEEE/CVF Conference on Computer Vision and Pattern Recognition (CVPR)*, pages 21719–21728. IEEE, 2024. 1
- [26] Yuke Li, Xiang Cheng, Yang Cao, Dexin Wang, and Liuqing Yang. Smart choice for the smart grid: Narrowband internet

- of things (nb-iot). *IEEE Internet of Things Journal*, 5(3): 1505–1515, 2017. 1
- [27] Zikun Liu, Gagandeep Singh, Chenren Xu, and Deepak Vasisht. Fire: enabling reciprocity for fdd mimo systems. In *Proceedings of the 27th Annual International Conference on Mobile Computing and Networking*, pages 628–641, 2021. 2
- [28] Haofan Lu, Christopher Vatheuer, Baharan Mirzasoleiman, and Omid Abari. Newrf: A deep learning framework for wireless radiation field reconstruction and channel prediction. *arXiv preprint arXiv:2403.03241*, 2024. 1, 2
- [29] R. Ma, S. Zheng, H. Pan, et al. Automs: Automated service for mmwave coverage optimization using low-cost metasurfaces. In *Proceedings of the 30th Annual International Conference on Mobile Computing and Networking*, pages 62–76. ACM, 2024. 1
- [30] JR Mahan, NQ Vinh, VX Ho, and NB Munir. Monte carlo ray-trace diffraction based on the huygens–fresnel principle. *Applied optics*, 57(18):D56–D62, 2018. 3
- [31] James Clerk Maxwell. *A treatise on electricity and magnetism*. Clarendon press, 1873. 1
- [32] Ben Mildenhall, Pratul P Srinivasan, Matthew Tancik, Jonathan T Barron, Ravi Ramamoorthi, and Ren Ng. Nerf: Representing scenes as neural radiance fields for view synthesis. *Communications of the ACM*, 65(1):99–106, 2021. 1, 2
- [33] Han Na and Thomas F Eibert. A huygens’ principle based ray tracing method for diffraction calculation. In *2022 16th European Conference on Antennas and Propagation (EuCAP)*, pages 1–4. IEEE, 2022. 1
- [34] Michael Niemeyer, Fabian Manhardt, Marie-Julie Rakotsaona, Michael Oechsle, Daniel Duckworth, Rama Gosula, Keisuke Tateno, John Bates, Dominik Kaeser, and Federico Tombari. Radsplat: Radiance field-informed gaussian splatting for robust real-time rendering with 900+ fps. *arXiv preprint arXiv:2403.13806*, 2024. 1
- [35] Tribhuvanesh Orekondy, Pratik Kumar, Shreya Kadambi, Hao Ye, Joseph Soriaga, and Arash Behboodi. Winert: Towards neural ray tracing for wireless channel modelling and differentiable simulations. In *The Eleventh International Conference on Learning Representations*, 2023. 2
- [36] Milica Đorđević, Nenad Jevtić, and Marija Malnar. Application of the sionna software for 5g/6g physical layer simulations. In *2024 32nd Telecommunications Forum (TELFOR)*, pages 1–4. IEEE, 2024. 9
- [37] Douglas Paul, Michel S Nakhla, Ramachandra Achar, and Andreas Weisshaar. Broadband modeling of high-frequency microwave devices. *IEEE transactions on microwave theory and techniques*, 57(2):361–373, 2009. 1
- [38] Roberto Pegurri, Francesco Linsalata, Eugenio Moro, Jakob Hoydis, and Umberto Spagnolini. Toward digital network twins: Integrating sionna rt in ns3 for 6g multi-rat networks simulations. *arXiv preprint arXiv:2501.00372*, 2024. 9
- [39] Clement Ruah, Osvaldo Simeone, Jakob Hoydis, and Bashir Al-Hashimi. Calibrating wireless ray tracing for digital twinning using local phase error estimates. *IEEE Transactions on Machine Learning in Communications and Networking*, 2024. 9
- [40] Chi-Jui Sung, Fan-Hao Lin, Tzu-Hao Huang, Chu-Hsiang Huang, Hui Chen, Chao-Kai Wen, and Henk Wymeersch. Communext: Deep learning-based cross-band and multi-directional signal prediction. *arXiv preprint arXiv:2511.05860*, 2025. 1
- [41] Nicolas Tsingos, Thomas Funkhouser, Addy Ngan, and Ingrid Carlbom. Modeling acoustics in virtual environments using the uniform theory of diffraction. In *Proceedings of the 28th annual conference on Computer graphics and interactive techniques*, pages 545–552, 2001. 3
- [42] Zhou Wang, Alan C Bovik, Hamid R Sheikh, et al. Image quality assessment: From error visibility to structural similarity. *IEEE Transactions on Image Processing*, 13(4):600–612, 2004. 6
- [43] Zhiqing Wei, Hanyang Qu, Yuan Wang, Xin Yuan, Huici Wu, Ying Du, Kaifeng Han, Ning Zhang, and Zhiyong Feng. Integrated sensing and communication signals toward 5g-a and 6g: A survey. *IEEE Internet of Things Journal*, 10(13): 11068–11092, 2023. 1
- [44] Chaozheng Wen, Jingwen Tong, Yingdong Hu, Zehong Lin, and Jun Zhang. Wrf-gs: Wireless radiation field reconstruction with 3d gaussian splatting. In *IEEE INFOCOM 2025 - IEEE Conference on Computer Communications*, pages 1–10, 2025. 1, 2, 4
- [45] Chaozheng Wen, Jingwen Tong, Yingdong Hu, Zehong Lin, and Jun Zhang. Neural representation for wireless radiation field reconstruction: A 3d gaussian splatting approach. *arXiv preprint arXiv:2412.04832v3*, 2025. 6
- [46] G. Wu, T. Yi, J. Fang, et al. 4d gaussian splatting for real-time dynamic scene rendering. In *Proceedings of the IEEE/CVF Conference on Computer Vision and Pattern Recognition*, pages 20310–20320. IEEE, 2024. 6
- [47] Kang Yang, Gaofeng Dong, Sijie Ji, Wan Du, and Mani Srivastava. Gsr: Complex-valued 3d gaussian splatting for efficient radio-frequency data synthesis. In *Proceedings of the 39th Conference on Neural Information Processing Systems (NeurIPS)*, 2025. 3, 6
- [48] Lihao Zhang, Haijian Sun, Samuel Berweger, Camillo Gentile, and Rose Qingyang Hu. Rf-3dgs: Wireless channel modeling with radio radiance field and 3d gaussian splatting. *arXiv preprint arXiv:2411.19420*, 2024. 1, 2, 3
- [49] Xiaoyu Zhang, Weihong Pan, Chong Bao, Xiyu Zhang, Xiaojun Xiang, Hanqing Jiang, and Hujun Bao. Lookcloser: Frequency-aware radiance field for tiny-detail scene. *arXiv preprint arXiv:2503.18513*, 2025. 1
- [50] Xiaopeng Zhao, Zhenlin An, Qingrui Pan, and Lei Yang. Nerf2: Neural radio-frequency radiance fields. In *Proceedings of the 29th Annual International Conference on Mobile Computing and Networking*, pages 1–15, 2023. 1, 2, 4, 6

Wideband RF Radiance Field Modeling Using Frequency-embedded 3D Gaussian Splatting

Supplementary Material

A. NVIDIA Sionna Simulator

NVIDIA Sionna is a machine learning-powered, GPU-accelerated PHY-layer communication simulation library designed for 6G research integrating AI and wireless networks. It enables high-fidelity modeling of advanced wireless channels (including millimeter wave, massive MIMO, and reconfigurable intelligent surfaces), supports seamless integration with ray tracing and 3D scene reconstruction technologies, and facilitates full-stack simulations encompassing multi-user MIMO systems, channel coding/decoding (e.g., LDPC, Polar codes), and adaptive modulation. Deeply integrated with TensorFlow/PyTorch frameworks, the simulator empowers end-to-end co-optimization of AI algorithms and communication systems, providing academic and industrial researchers with a highly efficient and scalable platform for intelligent communication system development.

The Sionna simulation library supports importing and reading material configuration parameters for components in modeled scenarios. Users can either define custom materials or utilize common materials pre-provided by the Sionna library. When creating custom materials, users must specify the material's relative permittivity and conductivity. Additionally, they may define custom functions to precisely control how the material interacts with wireless signals (e.g., scattering, refraction). The library also offers predefined real-world materials, where Sionna automatically calculates relative permittivity and conductivity based on the scenario's operating frequency. Users can conveniently modify the wireless signal frequency through the **scene.frequency** parameter to adapt material properties dynamically.

B. Description of the six 3D scenes

Fig. 5 illustrates 6 common indoor scenarios used in the experiments. Scenarios 1 and 6 are sparsely arranged to simulate simplified indoor environments, while the remaining scenarios are more densely populated with objects, serving to evaluate the model's performance on PAS prediction tasks under complex spatial conditions.

These scenarios are constructed in Blender to simulate a simplified residential environment. The receiver antenna array is fixed in a central position in the scene, while transmitter antenna samples are uniformly distributed across the three-dimensional space. The Channel Impulse Response (CIR) data corresponding to each transmitter position is cal-

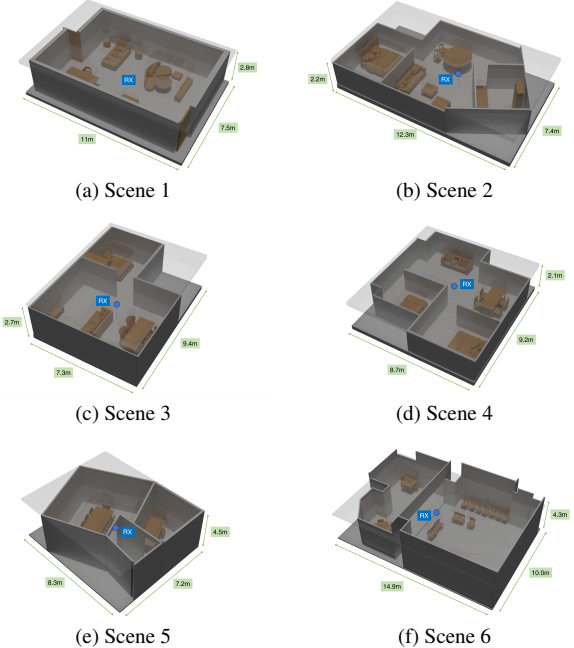


Figure 5. The 6 scenes used for dataset generation and experiments. The blue circular mark indicates the position of RX.

culated by ray tracing algorithm, then used for PAS generation.

C. Selected frequencies in wideband

We select 10 commonly used wireless signal frequencies in the daily scenarios and their representative applications. The specific frequency configurations employed in the experimental setup are determined based on this Tab. 6.

D. Power angular spectrum generation

The Bartlett beamforming algorithm is employed to generate the power angular spectrum through three coordinated processing stages. First, **theoretical phase field construction**: this stage establishes the array manifold by calculating the theoretical phase differences for incident plane waves from all scanning angles (azimuth and elevation) relative to the arbitrary 3D antenna coordinates. Second, **aggregated phase extraction**: to address multipath fading and isolate the coherent signal component, the algorithm employs a complex summation strategy. This process aggregates the CIR across all resolved multipath components using coherent addition, which constructively reinforces the

Table 6. The 10 selected radio frequencies and their typical applications.

Freq. Band (GHz)	Selected Freq. (GHz)	Typical Applications
0.9 – 1.0	1.0	FM Radio, AM Radio
2.4 – 2.5	2.4	Wi-Fi (802.11b/g/n), Bluetooth, Zigbee, Microwave Ovens
5.0 – 5.9	5.0	Wi-Fi (802.11a/n/ac), 5G NR (New Radio), Short-Range Radar
8.0 – 10.0	10.0	Military Radar, Satellite Communication, Weather Radar
24.25 – 27.5	24.25	5G, Point-to-Point Communication
37.0 – 40.0	37.0	5G, Automotive Radar, Industrial Sensors
47.0 – 50.0	47.0	5G, Satellite Communication, Point-to-Point Links
57.0 – 64.0	60.0	WiGig (802.11ad), Short-Range Wireless Communication
76.0 – 81.0	77.0	Automotive Radar, 5G, Short-Range Communication
92.0 – 95.0	94.0	Radar Systems, High-Resolution Imaging, 5G

Algorithm 1: Bartlett Power Angular Spectrum Generation

Input : \mathbf{H} : Channel matrix ($N_{ant} \times L$ paths);
 \mathbf{P}_{ant} : 3D Antenna coordinates;
 $(\theta_{grid}, \phi_{grid})$: Angular search grid (N_{grid} points);
Output: \mathbf{S}_{spec} : Normalized Spatial Spectrum;
// 1. Compute theoretical phase manifold

- 1 Calculate direction vectors \mathbf{d}_k for all grid points
 $k \in \{1, \dots, N_{grid}\}$;
- 2 Compute path length differences:
 $\Delta \mathbf{R} \leftarrow \mathbf{P}_{ant}^T \cdot [\mathbf{d}_1, \dots, \mathbf{d}_{N_{grid}}]$;
- 3 $\Phi_{theo} \leftarrow -\frac{2\pi}{\lambda} \Delta \mathbf{R}$; // Theory phase
 $\in \mathbb{R}^{N_{ant} \times N_{grid}}$
// 2. Extract aggregated phases
- 4 Integrate multipath components via complex sum:
 $\mathbf{h}_{agg} \leftarrow \sum_{l=1}^L \mathbf{H}[:, l]$; // Result $\in \mathbb{C}^{N_{ant}}$
- 5 Extract phase from the aggregated signal:
 $\psi_{raw} \leftarrow \angle(\mathbf{h}_{agg})$;
- 6 Normalize to remove common offset:
 $\psi_{meas} \leftarrow \psi_{raw} - \text{mean}(\psi_{raw})$; // Measured phase $\in \mathbb{R}^{N_{ant}}$
// 3. Synthesize PAS
- 7 **foreach** angle index k in grid **do**
- 8 Calculate phase deviation between theory and measurement: $\delta_k \leftarrow \Phi_{theo}[:, k] - \psi_{meas}$;
- 9 Perform coherent array integration
(Beamforming): $V_k \leftarrow \sum_{n=1}^{N_{ant}} \exp(j \cdot \delta_k[n])$;
- 10 Compute magnitude response: $\mathbf{S}_{raw}[k] \leftarrow |V_k|$;
- 11 Apply Min-Max normalization:
 $\mathbf{S}_{spec} \leftarrow \mathbf{S}_{raw} / \max(\mathbf{S}_{raw})$;
- 12 **return** \mathbf{S}_{spec} ;

dominant signal while suppressing noise. The phase of this aggregate complex vector is then extracted and normalized by removing the mean phase offset to obtain the relative spatial phase variations across the antenna array. Finally, **PAS synthesis:** the algorithm reconstructs the angular spectrum by computing the spatial coherence between the extracted measurement phases and the theoretical phase field. By calculating the phase deviation for each scanning angle and performing coherent integration across the antenna aperture, the algorithm generates a spatial response map, which is subsequently normalized to visualize the Direction of Arrival (DoA) distribution.

The pseudocode is shown in algorithm 1:

E. Dataset split protocols

E.1. Dataset for overall evaluation

For the overall evaluation in Sec. 5.2, we train one wideband model using PAS at 10 frequencies in each scenario, with 80% PAS at each frequency for training and other 20% at each frequency for test. The TX positions of PAS in the test set are completely non-repetitive of those in the training set. We train 10 WRF-GS+ and 10 GSRF baselines using PAS at each individual frequency, each with 80% for training and 20% for test.

E.2. Dataset for cross-frequency prediction

For the cross-frequency prediction in Sec. 5.3, we train wideband models using different frequency combinations of the 10 frequencies. The frequencies are listed in Tab. 7. Combinations C1-C3 progressively reduce the number of training frequencies (from 5 to 2 frequencies) while expanding the testing range (from 5 to 8 frequencies). The training frequencies include the left boundary of 1GHz and the right boundary of 94GHz, along with optional intermediate frequencies. The remaining frequencies, distributed among these training frequencies, are used for test.

Table 7. Combinations of 10 frequencies for cross-frequency prediction.

Combination	# of training freq.	Training freq. (GHz)	# of test freq.	Testing freq. (GHz)
C1	5	1, 5, 24.25, 47, 77	5	2.4, 10, 37, 60, 94
C2	3	1, 24.25, 94	7	2.4, 5, 10, 37, 47, 60, 77
C3	2	1, 94	8	2.4, 5, 10, 24.25, 37, 47, 60, 77

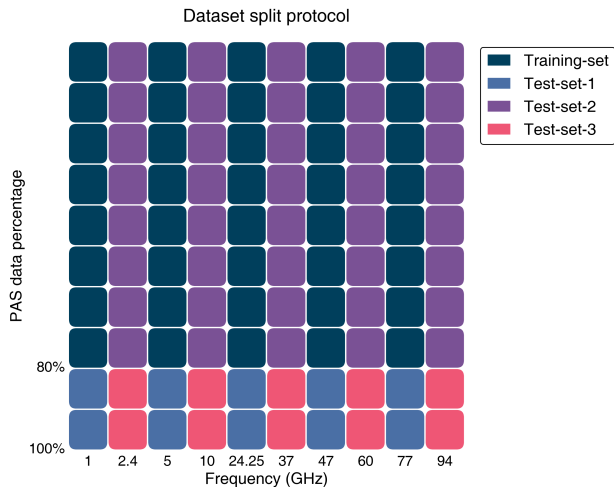


Figure 6. The dataset split protocol for PAS prediction of unseen TX positions, unseen frequencies and both.

Table 8. Detailed description for the dataset split protocol.

Combination	Frequency	TX position
Training-set	Known	Known (80%)
Test-set-1	Known	Unknown (20%)
Test-set-2	Unknown	Known (80%)
Test-set-3	Unknown	Unknown (20%)

E.3. Dataset for unseen positions and frequencies

For the evaluation for unseen positions and frequencies in Sec. 5.4, we split the whole dataset in each scenario into one training set and three test sets. The training set contains 5 frequencies out of the 10 frequencies, with 80% PAS samples. Test-set-1 contains the remaining 20% PAS samples of these 5 frequencies (i.e. known frequency, unknown position). Test-set-2 contains other 5 untrained frequencies with 80% PAS samples (i.e. unknown frequency, known position). Test-set-3 contains the last 20% PAS samples at those 5 untrained frequencies (i.e. unknown frequency, unknown position). This dataset split protocol is illustrated in Fig. 6 and summarized in Tab. 8.

F. Detailed structure of EM feature network

The detailed network structure design of the EM Feature Network is shown in Tab. 9. The network consists of 3 embedders and several Fully-Connected (FC) layers. Layer 4 generates the attenuation factors and hidden EM feature vectors based on the input Gaussians and the signal frequency. Layer 7 produces signal factors attribute by processing the hidden EM feature vectors, the input Gaussians, the signal frequency and the TX position.

G. Training implementation

Our wideband model is implemented in Python (full code and dataset will be publicly accessible upon acceptance of the work) and trained on an NVIDIA A800 GPU with 80GB of graphics memory.

Tab. 10 lists the hyperparameter settings for the implementation of our wideband model. For the WRF-GS+ and GSRF baseline models, we use the default configurations from their official Python implementations on Github.

For efficiency comparison in Sec. 5.5, we summarized the average time for model training for 200k iterations, the average time for the entire inference process to predict a PAS (including network forwarding and CUDA rendering), and the average time for only CUDA rendering.

Table 9. Details of EM Feature Network.

Layer ID	Operation	Input dim	Output dim
Gaussian Embedder	Embedding Gaussians	Gaussian coordinate dim (3)	$Emb(Gaus)$ dim (63)
Frequency Embedder	Embedding frequency	Frequency dim (1)	$Emb(freq)$ dim (13)
TX Position Embedder	Embedding TX position	TX position dim (3)	$Emb(P_{TX})$ dim (39)
Freq Layer 0	FC layer	$Emb(freq)$ dim (13)	Hidden layer width (64)
Freq Layer 1	FC layer	Hidden layer width (64)	$Emb(freq)$ dim (30)
TX Layer 0	FC layer	$Emb(P_{TX})$ dim (39)	Hidden layer width (256)
TX Layer 1	FC layer	Hidden layer width (256)	$Emb(P_{TX})$ dim (90)
Layer 0	FC layer	$Emb(Gaus)$ dim (63) + $Emb(freq)$ dim (30)	Hidden layer width (256)
Layer 1	FC layer	Hidden layer width (256)	Hidden layer width (256)
Layer 2	FC layer	Hidden layer width (256)	Hidden layer width (256)
Layer 3	FC layer	Hidden layer width (256)	Hidden layer width (256)
Layer 4	FC layer	Hidden layer width (256)	Hidden layer width (256)
Attenuation output layer	Linear	Hidden layer width (256, from Layer 4)	Attenuation factor dim (1)
Layer 5	Residual layer	$Emb(Gaus)$ dim (63) + $Emb(freq)$ dim (30) + $Emb(P_{TX})$ dim (90) + Hidden layer width (256)	Hidden layer width (256)
Layer 6	FC layer	Hidden layer width (256)	Hidden layer width (256)
Layer 7	FC layer	Hidden layer width (256)	Hidden layer width (256)
Signal output layer	Linear	Hidden layer width (256, from Layer 7)	Signal factor dim (3)

Table 10. Detailed hyperparameter settings for model training.

Hyperparameter	Annotation	Value
ϵ_{dens}	Threshold of position gradient for Gaussian densification	0.0002
ϵ_{δ}	Threshold of attenuation to remove Gaussian	0.005
N_{dens}	Iteration interval for Gaussian densification	100
N_{reset}	Iteration interval for Gaussian attenuation reset	3000
lr_{sig}	Learning rate for Gaussian’s signal attribute	0.0025
lr_{att}	Learning rate for Gaussian’s attenuation attribute	0.025
lr_{scal}	Learning rate for Gaussian’s scaling attribute	0.05
lr_{rot}	Learning rate for Gaussian’s rotation attribute	0.01
lr_{init}	Initial learning rate for the EM network	1.6×10^{-4}
lr_{final}	Final learning rate for the EM network	1.6×10^{-6}
λ	Weight for SSIM loss	0.2
λ_{δ}	Weight for L2 penalty	0.01
Iter	Training iterations	200000